Journal of Civil Structural Health Monitoring
https://doi.org/10.1007/s13349-024-00842-5

ORIGINAL PAPER

Over 25-year monitoring of the Tsing Ma suspension bridge in Hong Kong

Lu Zhang[1,2] · Tian Lu[1,2] · Fei Wang[1,2] · Yong Xia[1,2]

Received: 7 May 2024 / Accepted: 8 August 2024

Abstract
Bridges in service are subjected to environmental and load actions, but their status and conditions are typically unknown. Health monitoring systems have been installed on long-span bridges to monitor their loads and the associated responses in real time. Since 1997, the Tsing Ma suspension bridge in Hong Kong has been the world's first of the type equipped with a long-term health monitoring system. For the first time, this study reports the first-hand field monitoring data of the bridge from 1997 to 2022. The 26-year data provide an invaluable and rare opportunity to examine the long-term characteristics of the loads, bridge responses, and their relationships, thereby enabling the assessment of the bridge's load evolution and structural condition over time. Results show that traffic loads have remained stable after 2007, highway vehicles kept increasing until the COVID-19 pandemic in 2020, the annual maximum deck temperature continued to increase at a rate of 0.51 °C/decade, typhoon durations increased by 2.5 h/year, and monsoon speeds decreased and became dispersed and variable. For the bridge responses, deck displacement is governed by the varying temperature. Natural frequencies in the past 26 years were almost unchanged. The overall condition of the bridge is very satisfactory. Current status and recent update of the health monitoring system are also reported. Lastly, prospects of bridge health monitoring are discussed. This study is the first to report the over one-quarter century status of a structural health monitoring system and the behavior of a long-span suspension bridge. This research provides a benchmark for many other bridge monitoring systems worldwide.

Keywords Structural health monitoring · Long-span bridges · Long-term behavior · Load evolution

1 Introduction

Long-span bridges serve as lifeline structures in transportation networks and are critical to the economies of various countries. Their @@failure can be catastrophic in terms of life losses and economic and social impact [1, 2]. Throughout the service life of bridges, they are subject to complex loadings and hazards (e.g., typhoons and earthquakes) and exposed to harsh environments (e.g., corrosion) [3, 4]. Therefore, long-span bridges should meet the functionality requirements under operational loads and safety requirements under extreme events [5]. The 2021 ASCE Report Card [6] shows 7.5% bridges in the US are in "poor" condition and require $125 billion in repairs. In this regard, understanding and assessing structural functionality and safety conditions in real time, alerting the owners as early as possible for potential damage, and formulating a cost-effective maintenance strategy are important.

Systematic inspections of bridges began after the collapse of a bridge at Point Pleasant, US, in 1967 [7]. Since then, the structural health monitoring (SHM) technology has undergone continuous development over time [3, 4, 8–12]. The SHM technology is now recognized as crucial for assessing structural serviceability and safety, guiding effective maintenance programs, and early warning to prevent failures

✉ Yong Xia
ceyxia@polyu.edu.hk

Lu Zhang
lu1zhang@polyu.edu.hk

Tian Lu
tian1.lu@connect.polyu.hk

Fei Wang
felixwf.wang@polyu.edu.hk

[1] Department of Civil and Environmental Engineering, The Hong Kong Polytechnic University, Hong Kong, People's Republic of China

[2] Joint Research Centre for Marine Infrastructure, The Hong Kong Polytechnic University, Hong Kong, People's Republic of China

Published online: 19 August 2024

[13–16]. In addition, the SHM technology plays a valuable role in establishing long-term historical databases and providing design guidance for the construction of new bridges [17–19].

Since the 1990s, SHM systems have been successfully implemented on numerous long-span bridges [20–24], such as Tsing Ma Suspension Bridge in Hong Kong, China, Akashi Kaikyo Bridge [25] in Japan, Runyang Bridge [23] in China, Great Belt East Bridge [26] in Europe, and Golden Gate Bridge [27] in the US [28]. The design of bridge SHM system has been incorporated into new bridge designs, such as Sutong Bridge [22] and Stonecutters Bridge [29]. Their SHM systems were accomplished in synchronism with construction and can provide these bridges "birth" archives. The newly constructed Governor Mario M. Cuomo Bridge is equipped with the largest and most complex SHM system of its kind in the US, providing real-time feedback on such aspects as pier and pylon tilt, deformation and settlement, and reinforcement corrosion rates [30]. In summary, SHM technologies are increasingly being applied to long-span bridges and have shown their effectiveness in ensuring structural serviceability and safety.

However, most SHM systems have only been in operation for a relatively short period. Available literature has only reported several years (typically 1–2 years) of observations, which may not capture the long-term deteriorations or degradation of bridges because their service life is generally around 100 years or even longer. Moreover, long-span bridges generally have been designed and constructed carefully owing to large investments. Their failure or deterioration during the first several service years is rare. In addition, the status of these SHM systems after years of operation has not been reported either.

Tsing Ma Bridge has been equipped with a state-of-the-art SHM system since its operation in 1997 [31, 32], which is the first comprehensive system of its kind worldwide. The SHM system has been in continuous operation for over a quarter century. The field monitoring data of the system have been adopted to study the load effects of the bridge caused by highway, railway, wind, and temperature [9]. Similar to other SHM systems, the long-term data and bridge behavior have not been studied.

This study conducts an extensive analysis on the data measured by the SHM system of Tsing Ma Bridge over the past 26 years from 1997 to 2022. First, the development of the SHM system in Hong Kong is reviewed. Second, Tsing Ma Bridge and the SHM system, as well as their current status and recent update, are introduced. Third, in-depth analysis is performed on the monitoring dataset, consisting of three aspects: (1) long-term trends for key bridge loads, including wind, temperature, train, and vehicle loads; (2) long-term structural performance of the bridge, such as deformations, natural frequencies, and fatigue damage of critical components; and (3) correlation analysis between external loads and structural responses, quantifying such relationships as temperature and deformation, wind and deformation, and temperature and modal characteristics. The results can be regarded as a benchmark of other long-span bridge monitoring systems.

2 Development of SHM systems in Hong Kong

The SHM systems for bridges in Hong Kong have undergone several generations of development over the past decades. The first generation of SHM systems was developed in the 1990s and implemented on major bridges, such as Tsing Ma, Ting Kau, and Kap Shui Mun. These early systems marked the transition from traditional manual bridge inspections toward sensor-based SHM systems, making Hong Kong at the forefront of SHM development. These first-generation systems focused on monitoring key parameters, such as wind speeds and deck movements. Data analysis is more manual, less integrated with advanced analytics, and relies heavily on the expertise of engineers. These systems were designed to utilize wired transmissions to identify problems and support routine maintenance.

In the 2000s, the second generation of SHM systems was applied on such bridges as Western Corridor Bridge [33] and Stonecutters Bridge [29]. These systems featured more comprehensive sensor networks, with Stonecutters Bridge alone incorporating 1571 monitoring sensors across 15 different types; this bridge may have the most number of sensors among all bridges. Advanced sensing technologies, such as video cameras, were also integrated, and corrosion sensors were installed to monitor the durability of the bridge. In addition, these systems introduced centralized data processing and control systems, enabling more advanced analytics compared with the previous generation [34]. The second generation of SHM in Hong Kong is a refinement and development of the first generation, marking the beginning of more intelligent and advanced technologies in the field of bridge health monitoring.

The latest, third-generation SHM systems in Hong Kong, which incorporate cutting-edge artificial intelligence (AI) and digital twin (DT) technologies, are currently under development. For example, cameras and weigh-in-motions are integrated to monitor the traffic load along the entire bridge using the computer vision technique [35–37]. Machine learning models are trained and embedded into the SHM system to automatically detect anomalies [38, 39]. Digital twins are virtual, data-driven models of the physical bridge structures. These models are continuously updated with real-time data from extensive sensor networks on the bridges. AI and DT-enhanced SHM systems can provide

comprehensive and real-time bridge information, including loading conditions and structural responses. The systems can also provide predictive analytics. They can predict future behaviors, estimate component life, and recommend optimal maintenance actions. With these new technologies, the latest SHM generation will assist in intelligent, data-driven bridge management in Hong Kong.

3 Tsing Ma Bridge and its SHM system

3.1 Introduction of Tsing Ma Bridge

Tsing Ma Bridge, connecting Tsing Yi Island and Ma Wan Island, is a dual-use suspension steel bridge for highways and railways. It has two highway carriageways on the upper deck and two rail lines and two emergency carriageways on the lower deck. The bridge has a main span of 1377 m and a total length of 2132 m. The height of the two towers is 206.4 m high with respect to the base level, as shown in Fig. 1 [40]. Tsing Ma Bridge was officially opened on May 22, 1997.

3.2 Overview of the SHM system on Tsing Ma Bridge

The SHM system was operated from 1997 [41]. The system consists of six module sensors, namely data acquisition and transmission, data processing and control, structural health evaluation, portable data acquisition, portable inspection, and maintenance system [9]. The sensor system deployed on Tsing Ma Bridge includes 283 sensors in 8 types, as listed in Table 1, in which the Global Positioning System (GPS) was integrated into the SHM system in 2001 [9, 42]. These sensors measure loads, such as wind, traffic, and temperature; and structural responses, such as acceleration, strain, and displacement. Additional details of the SHM system are provided in Xu and Xia [9].

3.3 Current status of the SHM system

The mean time between failures of the SHM system was designed to be 15–20 years. After 26 years of operation, sensor damage has occurred over time. Table 2 presents the number of damaged sensors after 15 years (2012), 20 years (2017), and 25 years (2022) of operation.

Table 2 shows that the sensors are generally in good operating condition. In particular, all anemometers and displacement transducers remaining are undamaged as of 2022. Comparatively, GPS exhibits the most severe damage, with 4 out of the 14 stations malfunctioning. Apart from GPS, the number of damaged thermometers increased from 6 in 2012 to 11 in 2022. Three strain gauges were damaged in 2012 and eight more in 2017. The damaged strain gauges

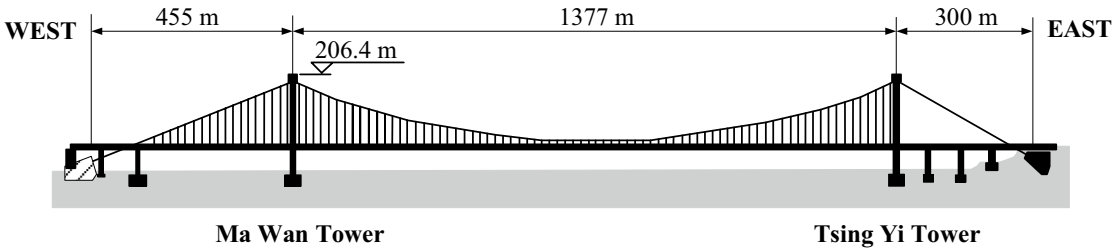

Fig. 1 Elevation of Tsing Ma Bridge

Table 1 Sensors deployed on Tsing Ma Bridge [9]

Monitoring items	Sensor types	No. of sensors	Positions
Wind speed and direction	Anemometer	6	2: deck of main span; 2: top of towers; 2: deck of Ma Wan side span
Temperature	Thermometer	115	6: ambient; 23: main cables; 86: deck section
Highway traffic	Weigh-in-motion station	7	Approach to Lantau Toll Plaza
Displacement	Displacement transducer	2	1: portal beam of Ma Wan tower; 1: deck at the Tsing Yi abutment
	GPS station	14	4: top of towers; 2: middle of main cables; 2: middle of the Ma Wan side span; 6: ¼, ½, and ¾ of the main span
	Level sensing station	10	1: abutment; 3: towers; 4: deck of the main span; 2: deck of the Ma Wan side span
Acceleration	Accelerometer	19	8: uni-axial, deck, and Tsing Yi tower; 9: bi-axial, deck, and main cables; 2: tri-axial, main cables, and the Ma Wan abutment
Strain	Strain gauge	110	29: Ma Wan side span; 49: main span; 32: cross frame at Ma Wan tower
Total		283	

Table 2 Sensor damage on Tsing Ma Bridge

Sensor types	No. of damaged sensors		
	2012	2017	2022
Anemometer	0/6	0/6	0/6
Thermometer	6/115	7/115	11/115
Displacement transducer	0/2	0/2	0/2
GPS station	1/14	1/14	4/14
Level sensing station	1/10	1/10	0/10
Accelerometer	0/19	0/19	1/19
Strain gauge	3/110	11/110	5/110

decreased to 5 in 2022 after an SHM system update. Damaged level sensing stations also decreased in 2022 compared with 2017.

3.4 Recent update to the SHM system

The SHM system has been updated in the following aspects:

- A ship impact detection alarm system was provided, comprising four CCTV cameras approaching the two towers and two loops of fiber optics running along the south and north sides of the deck. This system enables the rapid identification of fiber-break locations and distances for fast damage detection.
- An acoustic monitoring system was installed on the main cables to capture acoustic emission signal from broken wires.
- The rehabilitated GPS system was upgraded by integrating GPS, BeiDou, GLONASS, Galileo, and QZSS.
- The data transmission system was upgraded from a fiber optic "token ring" network to wireless.
- A customized operating system with graphical user interface was established. It includes various features, including multiple sensor type selection, graphical display of sensory data, and reporting function.

4 Monitoring of loads

4.1 Train load

The railway on Tsing Ma Bridge connects Hong Kong Airport to the MTR Hong Kong Station. The Tung Chung Line and Airport Express on the bridge began operation in late June and early July 1998, respectively. Considering that train loads are the primary source of fatigue for bridge railway, monitoring the distribution of train loads and bridge responses is crucial to ensure operational safety [43, 44]. Accordingly, a set of strain gauges has been installed on the bottom of the railway T-section to record railway strain responses. Train traffic flow data can be extracted from the measured strain signals [44].

The annual total number of trains in two directions (i.e., airport-bound and Kowloon-bound) crossing Tsing Ma Bridge from 1998 to 2022 is illustrated in Fig. 2. The total number of trains increased significantly in 2003 owing to the opening of the 4-lane track from Olympic to Lai King stations and the implementation of 8-car trains on the Tung Chung Line. Increases in 2006 and 2007 were caused by the Lantau Airport Railway K-Train being put into service on the Tung Chung Line. Thereafter, the train number remained stable until a significant decrease in 2020 caused by the COVID-19 pandemic but gradually recovered from 2020 to 2022. Annual trains increased from 65,666 in 1999 (average of 180 per day) to 199,745 in 2019 (547 per day), a threefold increase compared with the initial operational period. Data in 1998 are not compared because the trains were operated on 22 June 1998. Data in this year are not representable. In addition, compared with the original design of the bridge, the designed annual single-line load capacity of the railway was 51 billion kilograms [40], while the maximum value observed in 2019 was 38.25 billion kilograms.

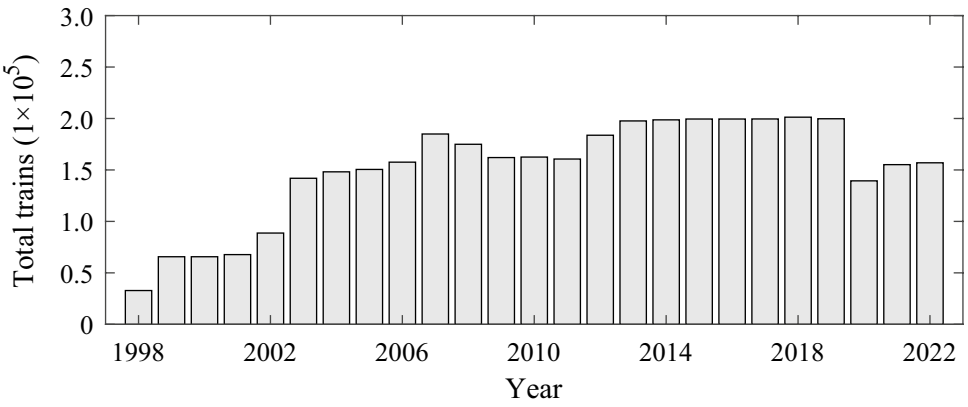

Fig. 2 Annual total trains crossing Tsing Ma Bridge from 1998 to 2022

4.2 Vehicle load

The hourly, daily, and monthly traffic statistics at the core station of the Lantau Line (from Tsing Ma Bridge eastern end at Tsing Yi to Ngong Shuen Au) are recorded [9]. The vehicles are categorized into 10 types: motorcycle, car, taxi, private light bus, public light bus, light goods vehicle, medium/heavy goods vehicle, coach, single-decked bus, and double-decked bus.

Figure 3 illustrates the annual total traffic flows across Tsing Ma Bridge in two directions from 1997 to 2022. The annual total number of vehicles crossing the bridge shows a consistent increase since its operation, reaching a peak in 2019. The total number of vehicles in 2019 (3.61×10^7, average of 98,787 per day) is almost four times the number recorded in 1998 (0.95×10^7, average of 26,041 per day). In 2020, the total number of vehicles decreased by half owing to the COVID-19 pandemic.

Among all vehicle types, cars and taxis showed the most significant increases before 2020. Their combined total number increased fivefold from 0.46×10^7 in 1998 (average of 12,488 per day) to 2.42×10^7 in 2019 (66,286 per day). In 2020, taxis experienced the sharpest decrease from 8.85×10^6 (24,252 per day) in 2019 down to 1.59×10^6 (4349 per day).

Figures 4 and 5 show the gross vehicle weight and lane distributions, respectively. In general, the proportion of vehicles decreases as gross vehicle weight increases. For the airport- and Kowloon-bound directions, vehicles are concentrated in the middle lane, with the proportion of vehicles in the fast lane close to that in the slow lane. Vehicles weighing below 4000 kg exceed 80% of the total vehicles and are most prevalent in the middle lane, followed by the fast lane, and least in the slow lane. By contrast, vehicles weighing over 4000 kg are concentrated in the slow lane, partially in the middle lane, and rare in the fast lane. Consequently, the slow lane may be subject to significant fatigue damage owing to traffic loads.

4.3 Temperature load

Temperature variations may have a more significant effect than operational loads, particularly for long-span bridges [45–47]. A total of 115 temperature sensors were installed on Tsing Ma Bridge to monitor temperature loads. The sensors include 6 ambient, 86 section, and 23 cable temperature sensors (denoted as P3, P1/P2/P4/P6, and TC, respectively)

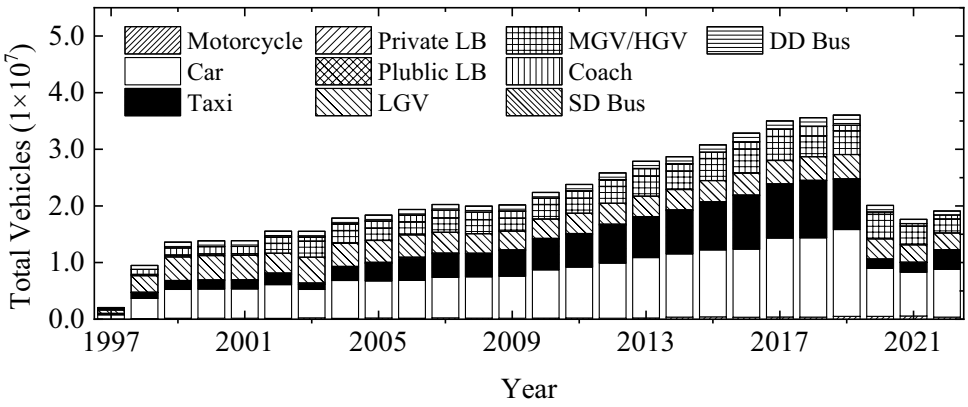

Fig. 3 Annual total number and composition of vehicles in 1997–2022

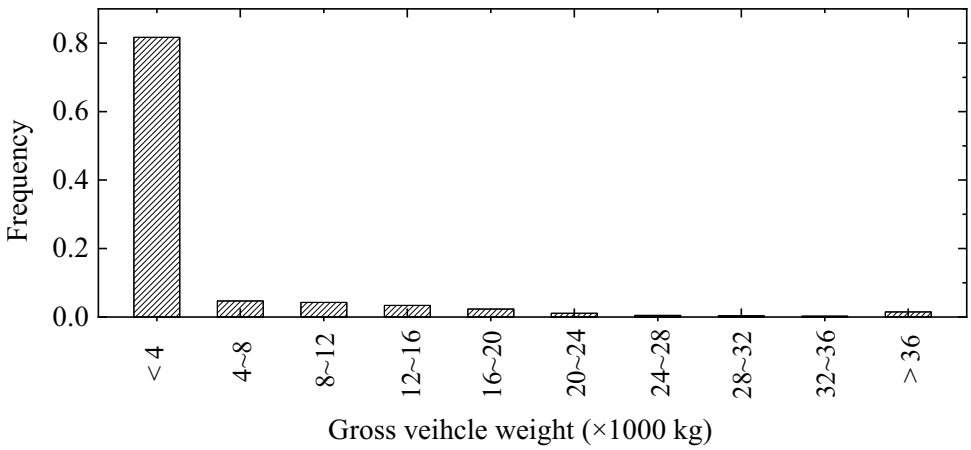

Fig. 4 Gross vehicle weight distribution

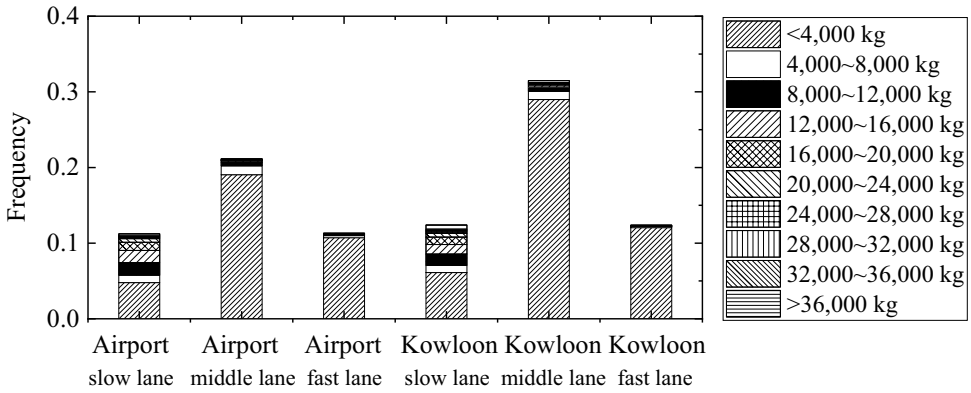

Fig. 5 Gross vehicle weight distribution on bridge lanes

[48], as shown in Fig. 6. All temperature sensors sample at a frequency of 0.07 Hz.

Figure 7 presents the monthly maximum, mean, and minimum effective temperatures of the Tsing Ma Bridge deck (Section O in Fig. 6) from 1997 to 2022. Ambient air temperature from sensor P3-TJS is also shown for comparison. The effective deck temperature is the area-weighted average temperature at multiple measurement points on the cross section.

The monthly effective temperature follows a similar seasonal variation as the ambient air temperature. The maximum effective temperature exceeds the air temperature by about 9 °C in the summer and 4 °C in the winter. The mean effective temperature is about 2 °C higher than the ambient air temperature. The minimum effective temperature closely aligns with the ambient air temperature.

Figure 8 shows the yearly maximum, mean, and minimum deck effective temperatures and ambient air temperatures. Linear regression analysis shows that the maximum deck effective and ambient temperatures increase at rates of 0.51 °C/decade and 0.72 °C/decade, respectively. Similarly, the increase rates of the mean deck effective and ambient temperatures are 0.16 °C/decade and 0.20 °C/decade, respectively; and those of the minimum deck effective and ambient temperatures are 0.20 °C/decade and 0.50 °C/decade. Therefore, the maximum deck effective temperature increases faster than the mean effective temperature. The results are also consistent with the records of the Hong Kong Observatory (HKO), which show an increase in temperature in Hong Kong over the past 30 years, as shown in Fig. 9. The maximum, mean, and minimum air temperatures in the last 30 years have been increasing at a rate of 0.74 °C/decade, 0.28 °C/decade, and 0.2 °C/decade, respectively.

The designed maximum and minimum effective temperatures of the deck are 46 °C and − 2 °C, respectively [9]. Although the measured effective temperatures remain within the design values, the annual maximum effective temperature is extremely close to the design limit. In particular, the maximum effective temperature in 2022 was 44.90 °C, just 1.10 °C below the design value. These temperature increases may be caused by global warming during the past decades, which has not been considered in the original design code. The IPCC AR6 report predicted that the global mean surface temperature could increase by about 1.85 °C and 3.55 °C by the end of twenty-first century compared with that in 1995–2014 under the intermediate (SSP2-4.5) and very high (SSP5-8.5) greenhouse gas emissions scenarios, respectively [49]. Therefore, the maximum effective temperature of the bridge may likely exceed the design value in the future because the maximum temperature increases faster than the mean value. If the trend in the past 26 years continues, then the maximum effective temperature of the bridge deck may reach the design value (46 °C) in 22 years (= 1.1/0.51 × 10). Although this case may not cause damage or failure of the bridge immediately, it reduces the reliability of the structure.

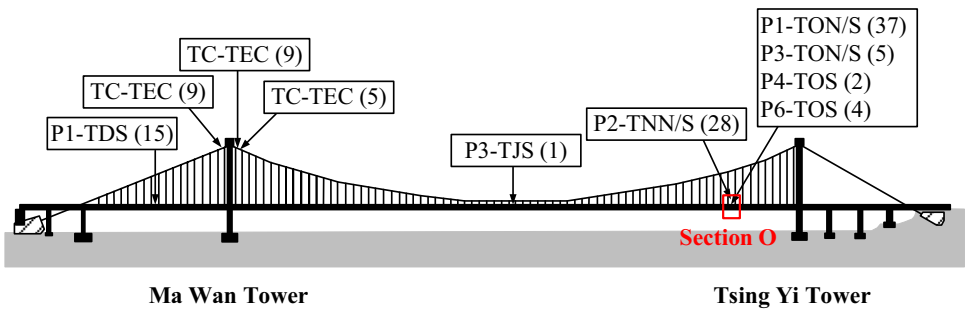

Fig. 6 Layout of the temperature sensors on Tsing Ma Bridge

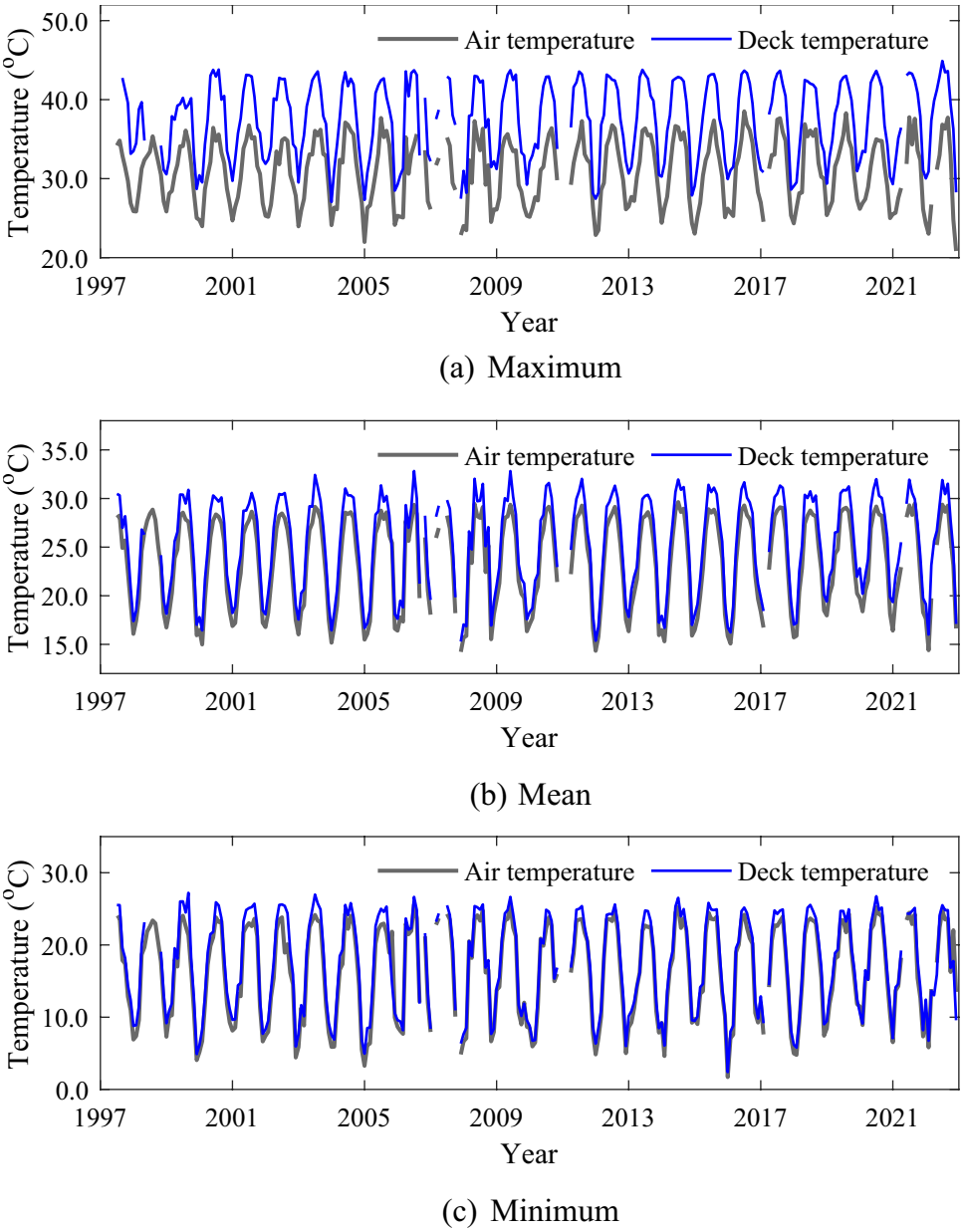

Fig. 7 Monthly ambient and deck effective temperatures in 1997–2022

Figure 10 illustrates the monthly maximum vertical temperature gradients on the south and north sides of the Tsing Ma Bridge deck (the bridge is approximately in the east–west direction). The gradients exhibit seasonal variations, reaching its peak in the summer at about 17 °C and minimum in the winter at about 8 °C. The south and north side gradients are relatively consistent in the winter, while the north side gradient is higher than the south side by 3 °C in the summer. The reason for this phenomenon is that the bridge is located south of the Tropic of Cancer, resulting in the direct solar radiation on the north side of the bridge during the summer, causing a higher temperature gradient on the north side.

4.4 Wind load

Tsing Ma Bridge has two types of wind environments: typhoons and monsoons. Monsoons are prevalent from November to April, while typhoons dominate the summer months. Six anemometers were installed on the bridge (Fig. 11), including two digital type Gill Wind Master ultrasonic anemometers in the middle of the main span (WI-TJS-01 and WI-TJN-01) and 4 analogue mechanical (propeller) anemometers on the tower and middle of the Ma Wan side span. The sampling frequency of anemometers is 2.56 Hz.

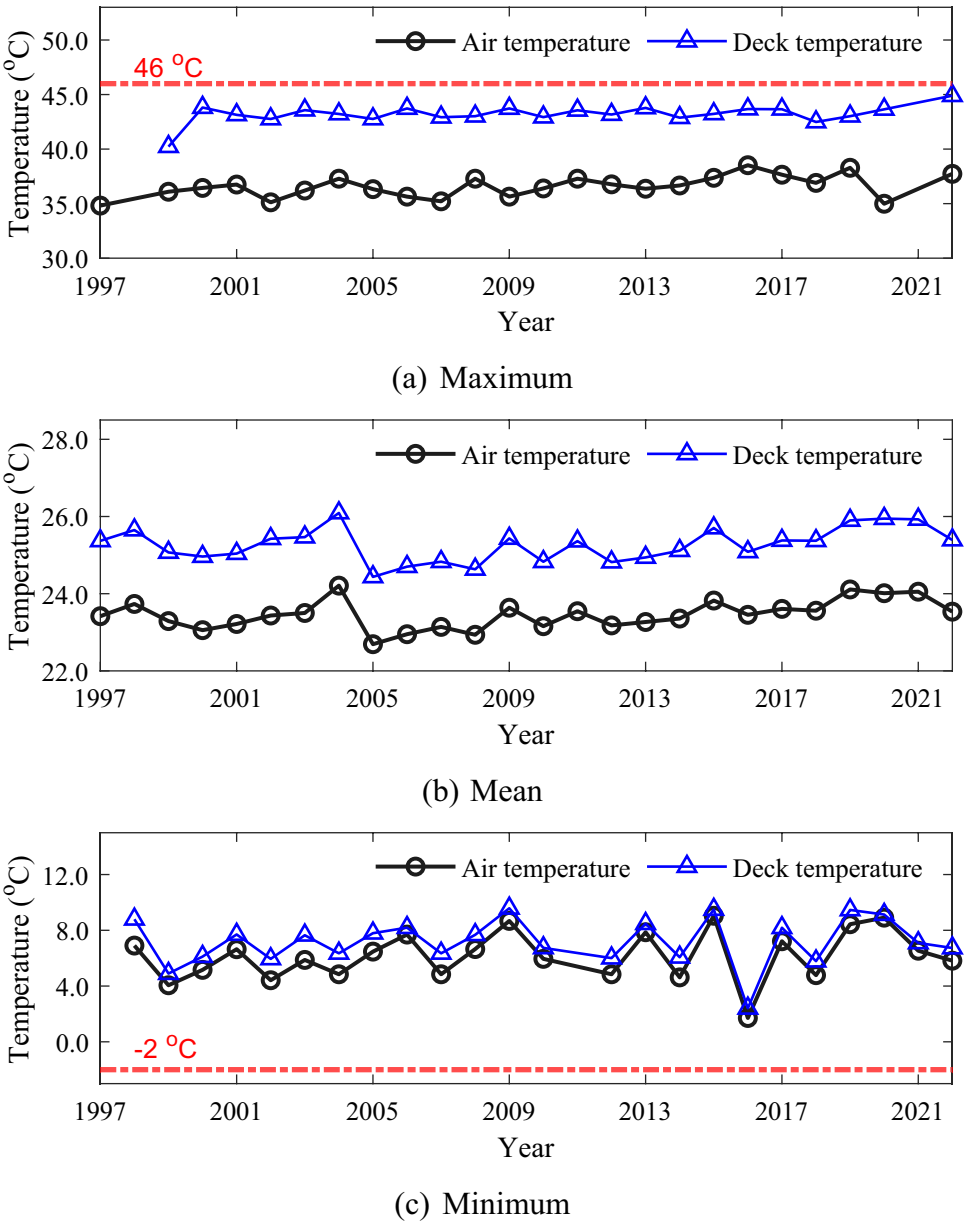

Fig. 8 Yearly ambient and deck effective temperatures in 1997–2022

4.4.1 Typhoon wind characteristics

Anemometer data in the typhoon periods from 2004 to 2022 are analyzed when HKO issued Tropical Cyclone Signal No. 3 or above. A total of 581 h of valid typhoon wind data are selected. Recorded wind speeds are categorized into four groups based on three thresholds: 10, 18, and 45.8 m/s [9].

Figure 12 presents the polar plot of the 10-min mean wind directions and speeds during typhoons. The predominant direction is from the NE direction, and wind speeds are concentrated within the range below 10 m/s. The maximum hourly mean wind speed observed over the past 26 years was 22.64 m/s, which is significantly lower than the designed threshold of 50 m/s [40].

Figure 13 plots the Weibull probability density functions (PDFs) of the 10-min mean wind speeds in three periods: 2006–2011, 2012–2016, and 2017–2022. Typhoon data for 2004–2005 are scarce and have not been used to consider long-term trends. This situation enables the analysis of long-term typhoon wind trends. The results show no significant trend in wind speed and distribution during a typhoon. Figure 14 shows the annual typhoon duration from 1997 to 2022 when the HKO issued Tropical Cyclone Signal No. 3 or above. According to linear regression, typhoon duration has an increasing trend of 2.5 h/year.

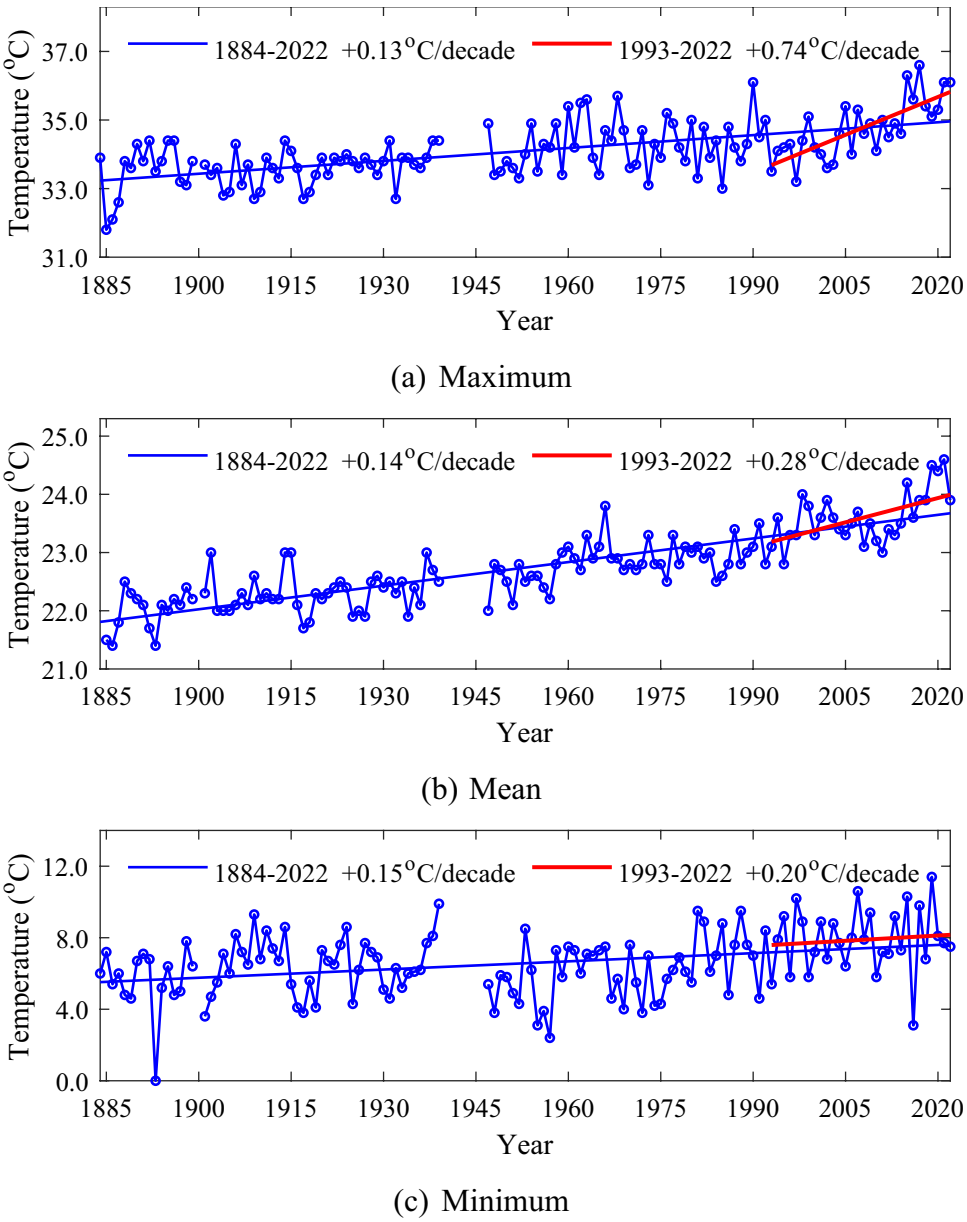

Fig. 9 HKO records of the annual maximum, mean, and minimum air temperatures in 1884–2022

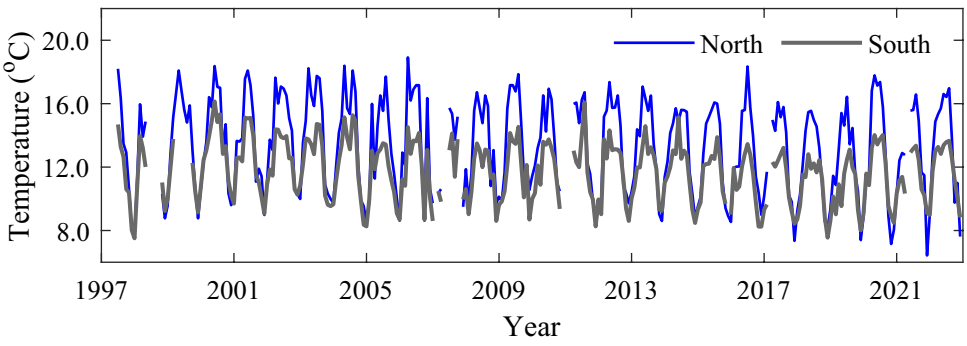

Fig. 10 Monthly maximum deck vertical temperature gradient

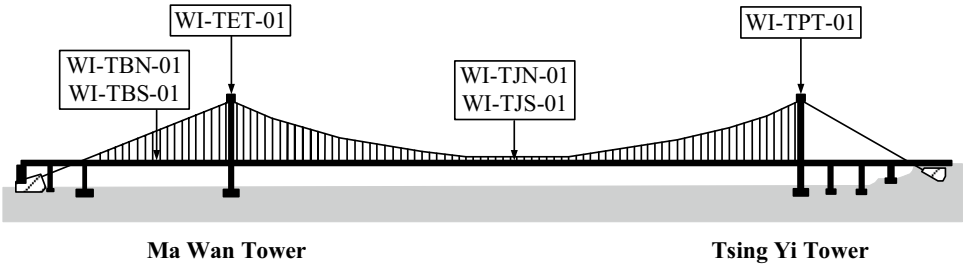

Fig. 11 Location of the anemometers on Tsing Ma Bridge

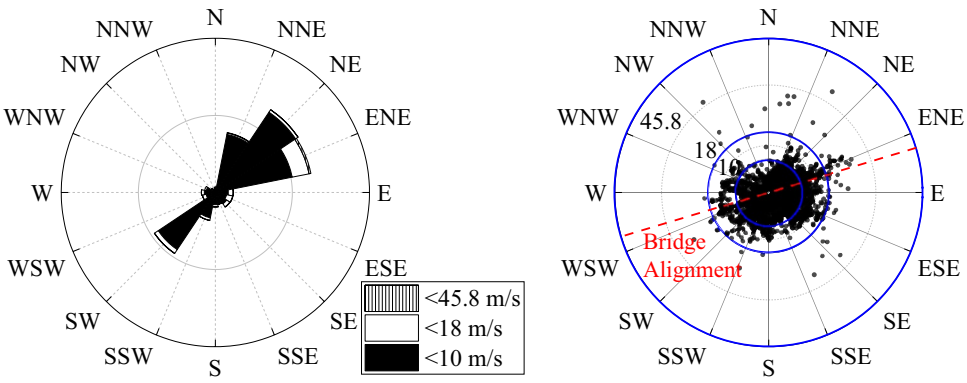

(a) Wind direction (b) Wind speed

Fig. 12 Polar plot of the 10-min mean wind direction and speed

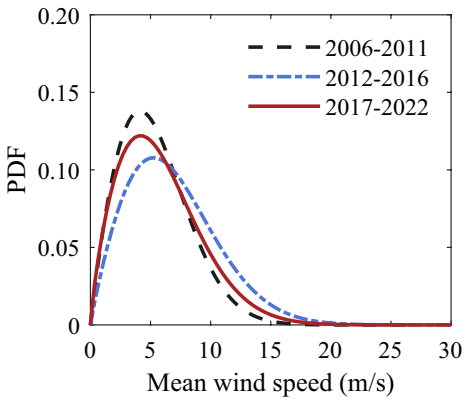

Fig. 13 Distribution of the 10-min mean wind speed during typhoons

4.4.2 Monsoon wind characteristics

The joint PDF (JPDF) of wind speed and direction is essential for evaluating wind-induced damage to bridges [9]. However, JPDF during the typhoon could not be obtained because of limited typhoon data. For monsoon, the Weibull function is adopted to fit wind speeds across all directions. Figure 15 presents the distributions of the 10-min mean wind speeds from all directions.

Figure 16 shows the Weibull scale and shape parameters fitted to the 10-min wind speeds across all directions during monsoons, as well as the relative frequency of wind directions. As shown in Fig. 16a, b, there is no significant relationship between the Weibull parameters and monsoon wind direction. The predominant monsoon wind direction is the

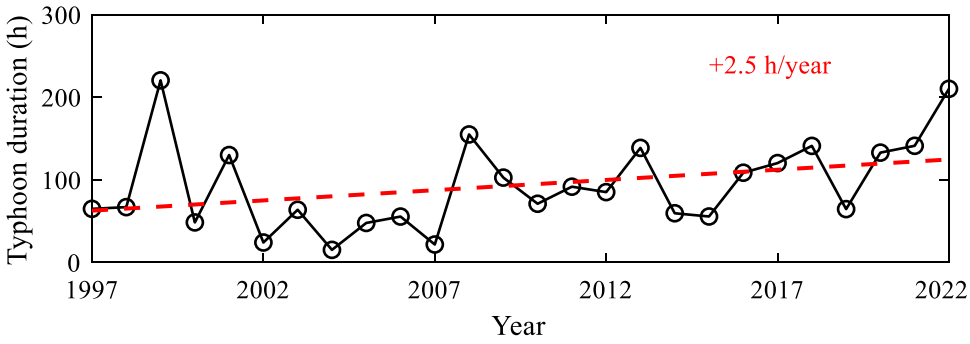

Fig. 14 Annual total typhoon duration from 1997 to 2022

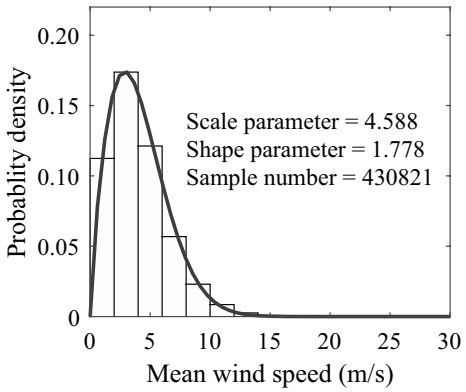

Fig. 15 Weibull distribution of the 10-min mean wind speed from all directions

ESE direction. In addition, winds from the east are more common than those from the west.

Figure 17 shows the Weibull scale and shape parameters from 2004 to 2022. The scale parameter, which represents the mean wind speed, shows a decreasing trend at a rate of 0.087/year. This result indicates that the monsoon wind speed distribution is shifting toward low values. Note that the shape parameter reflecting variability also shows a decreasing trend at a rate of 0.028/year. This result indicates that monsoon wind speeds have become markedly dispersed and variable.

The preceding findings align with observations from HKO, which has noted a weakening summer and winter monsoons affecting China in recent decades owing to global warming. Monsoon winds are caused by the temperature contrast between land and sea. Over the past few decades, the land has warmed more significantly than the oceans, and the temperature contrast between land and sea has decreased, leading to a weakening of the winter monsoon. The increase in anthropogenic aerosols reduces incoming sunlight, which decreases the temperature contrast between land and sea in the summer, thereby leading to a considerably weak summer monsoon [50].

Figure 18 shows the Weibull PDF plots of daily extreme wind speeds during monsoons in 2004–2009, 2010–2015, and 2016–2022 on Tsing Ma Bridge, revealing a declining trend in wind speeds from 2004 to 2022 during the monsoon. The results are also consistent with the observations in Fig. 17.

Fig. 16 Weibull scale and shape parameters and relative frequency of wind direction

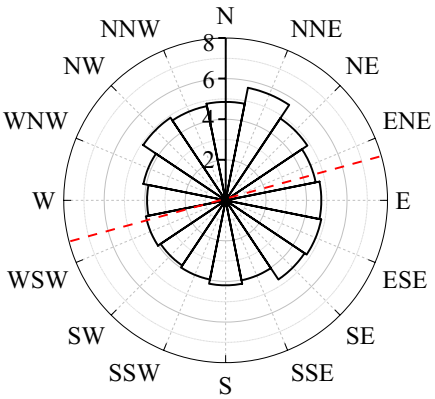

(a) Weibull scale parameter

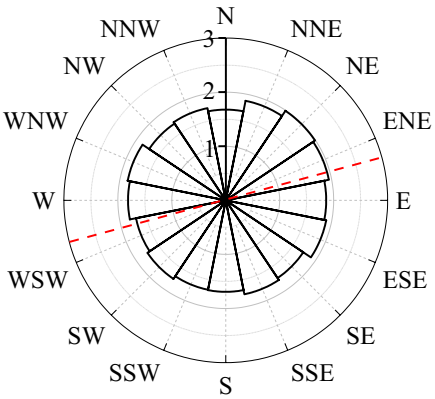

(b) Weibull shape parameter

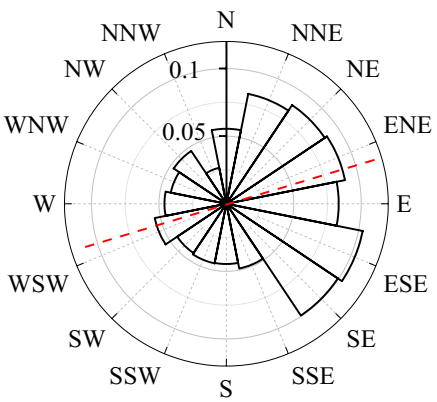

(c) Frequency of wind direction

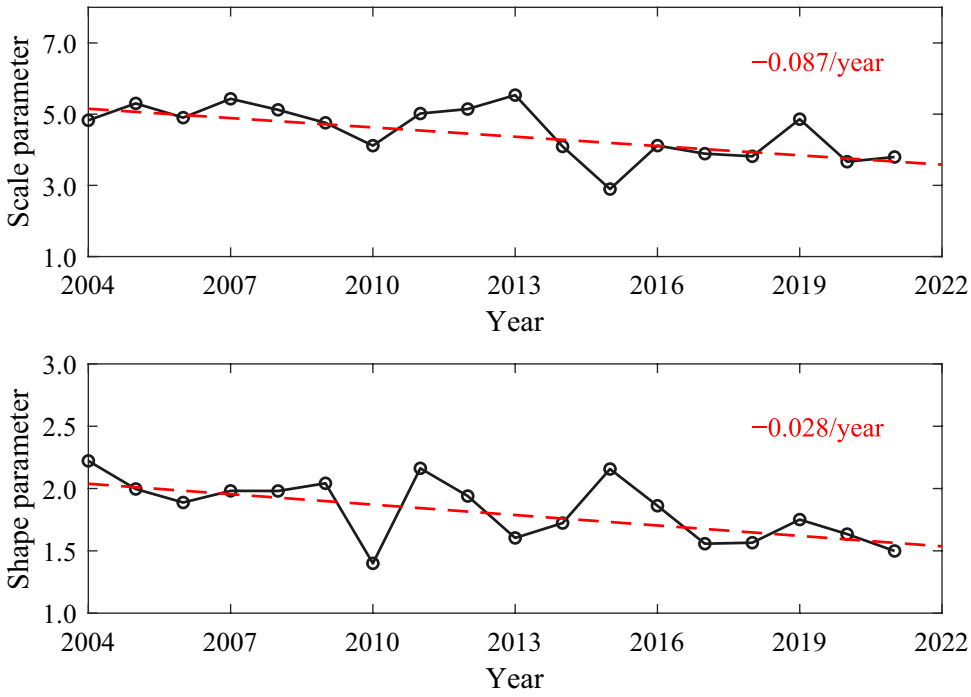

Fig. 17 Weibull scale and shape parameters from all directions in 2004–2022

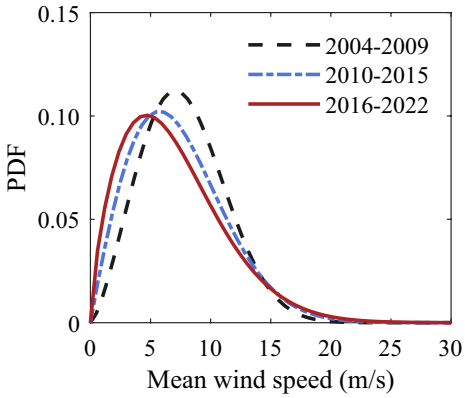

Fig. 18 Distribution of daily extreme wind speeds during monsoons

5 Monitoring of bridge responses

5.1 Displacement

5.1.1 Displacement sensor layout

The locations of level sensing stations, displacement transducers, and GPS stations on Tsing Ma Bridge are shown in Fig. 19. Level sensing stations (labelled as "LV") measure the vertical displacement of the bridge deck at multiple locations. The displacement transducer (DS-TRA-01) on the Tsing Yi side span measures the longitudinal displacement of the bridge deck, and another displacement transducer (DS-TEN-01) on the north side of a bearing frame measures the lateral bridge deck displacement. GPS stations (labelled as "TM") measure the lateral, vertical, and longitudinal displacements of the bridge deck, towers, and main cables at multiple locations.

5.1.2 Relationship between displacement and temperature

The relationship between the bridge deck effective temperature and displacement is explored in this section. A linear regression model can be expressed as follows [9]:

$$X = aT + b + \varepsilon, \tag{1}$$

where X and T are the bridge displacement and effective temperature, respectively, a and b are the coefficients, and ε is the fitting error.

The relationship between the daily mean mid-span deck deflection and effective temperature in 1997–2022 is shown in Fig. 20a, where upward and elongation displacements are positive. Applying Eq. (1) leads to $a = -48.11$ mm/°C, $b = 1412.32$ mm, and the coefficient of determination $R^2 = 0.890$. According to Zhou et al. [51], owing to the short length of the mid-span suspender, the temperature-induced mid-span deflection of a suspension bridge is almost equal to the displacement of the main cable, which can be simplified as follows:

$$D_V = \left(-\frac{3L}{16n} + \frac{h_{p1} + h_{p2}}{2}\right)\alpha, \tag{2}$$

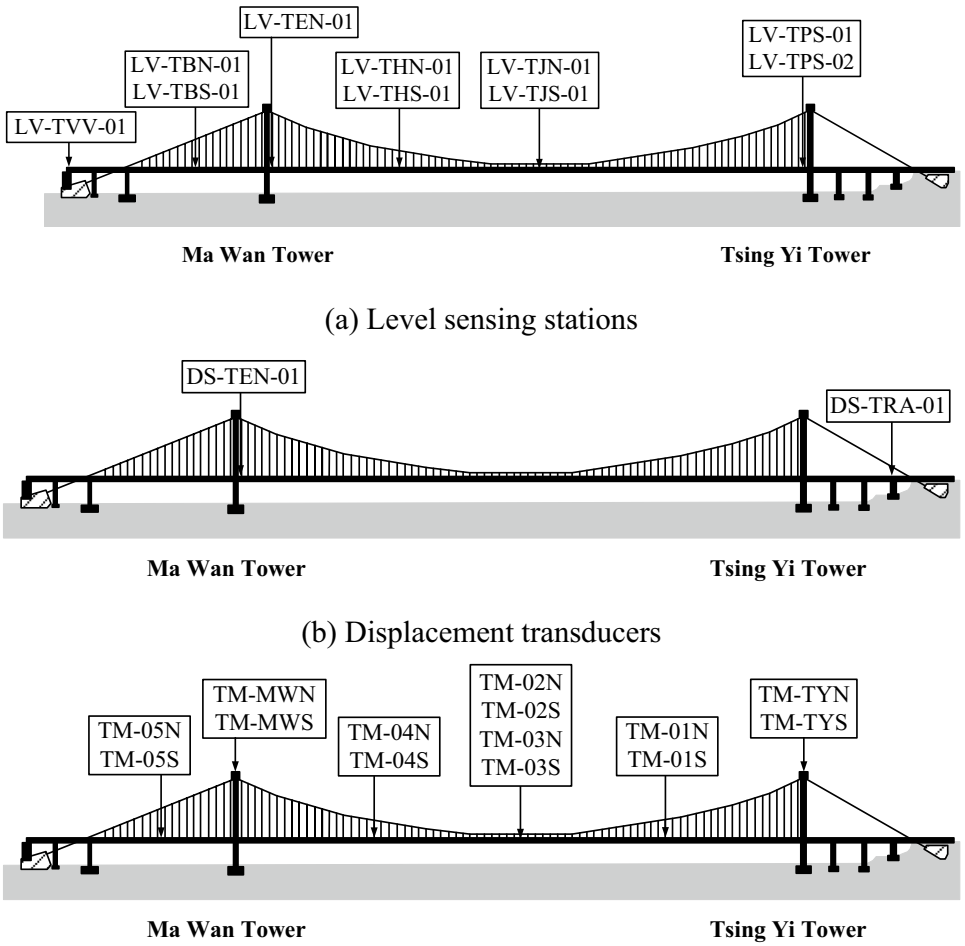

Fig. 19 Locations of the displacement sensors on Tsing Ma Bridge

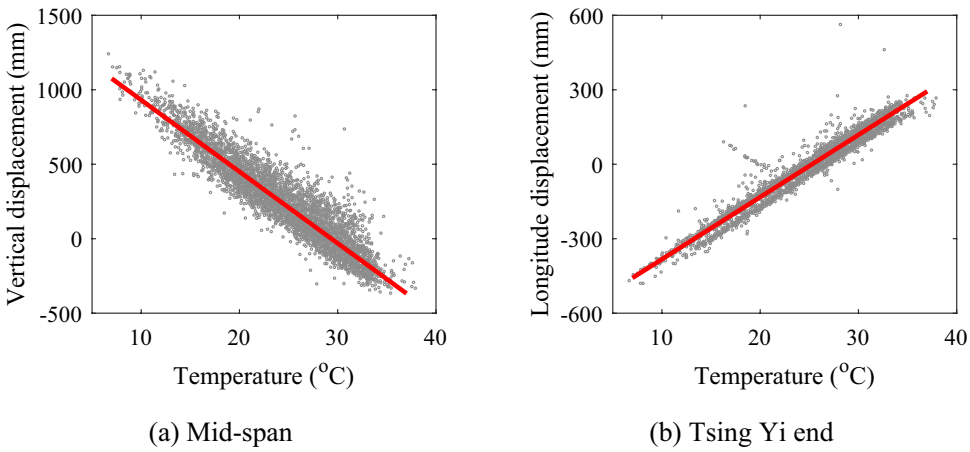

Fig. 20 Daily mean displacement versus deck effective temperature in 1997–2022

where L is the total length of the bridge, n is the sag ratio of the main cable, h_{p1} and h_{p2} are the height of the left and right towers, respectively, and α is the expansion coefficient. For Tsing Ma Bridge, $L = 2132$ m, $n = 0.091$, and $\alpha = 1.2 \times 10^{-5}$/°C. The calculated deflection of the mid-span is − 50.24 mm/°C, which is extremely close to the measured − 48.11 mm/°C. These results indicate that temperature is the primary contributor to the bridge vertical displacement.

The relationship between the longitudinal displacement at the Tsing Yi end and deck effective temperature is shown in Fig. 20b. According to Eq. (1), the coefficients

are $a = 25.52$ mm/°C, $b = -637.18$ mm, and $R^2 = 0.956$. Given that the bridge deck is fixed on the Ma Wan side and free to move on the Tsing Yi side, the unit temperature-induced longitudinal displacement at the Tsing Yi side can be calculated as follows:

$$D_{\mathrm{L}} = \alpha L_1, \tag{3}$$

where L_1 is the length between sensor DS-TRA-01 and the fixed end on the Ma Wan side, which is 2072 m. The calculated longitudinal displacement is 24.86 mm/°C, which is also extremely close to the measured 25.52 mm/°C.

5.1.3 Relationship between displacement and wind

As described by Xu and Xia [9], the lateral displacement of the bridge deck shows the evident correlation with the mean wind speed. Thus, the relationship between the wind and lateral displacement can be modeled using the following equation [19]:

$$D_w = cU^d, \tag{4}$$

where D_w is the 10-min lateral mean displacement, c and d are the fitting coefficients, and U is the 10-min mean wind speed. The 10-min mean wind speeds from the NNW direction over 5.0 m/s and corresponding bridge lateral displacements at four locations of the deck and main cable from 2011 to 2022 are utilized to establish Eq. (4). The fitted curves for the bridge deck and main cables at the mid-span are presented in Fig. 21. The regression coefficients are listed in Table 3. The regression coefficients d at four locations are 1.894, 1.760, 1.638, and 1.862, indicating that the mean lateral displacement is approximately proportional to the square of the 10-min mean wind speed. The results are also consistent with those of previous research [32].

Table 3 Regression coefficients in the wind direction sector NNW

GPS stations	Regression coefficients	
	c	d
TM-01	−0.578	1.894
TM-02	−1.265	1.760
TM-03	−1.552	1.638
TM-04	−0.734	1.862

5.1.4 Long-term displacement responses

Figure 22 shows the monthly mean mid-span deflection and longitudinal displacement at the Tsing Yi abutment from 1997 to 2022, in which GPS- and level sensing stations-measured mid-span deflection are displayed. The upward deflection and expansion of the longitudinal displacement are positive. The mid-span deflection of the GPS station and level station matches well, mutually verifying the reliability of the two displacement sensors for long-term monitoring. The vertical and longitudinal displacements exhibit evident seasonal variations caused by the temperature effect. The annual vertical movement at the mid-span is about 850 mm, and the longitudinal is approximately 400 mm.

5.2 Acceleration

5.2.1 Accelerometer layout

A total of 19 accelerometers are placed on Tsing Ma Bridge to monitor vibrations on the deck, cable, tower, and abutment. Figure 23 illustrates the sensor layout, where "AS," "AB," and "AT" denote uni-axial, bi-axial, and tri-axial accelerometers, respectively. Uni-axial accelerometers measure vertical vibration. Bi-axial sensors measure vertical and lateral vibrations. Tri-axial sensors record accelerations in three directions.

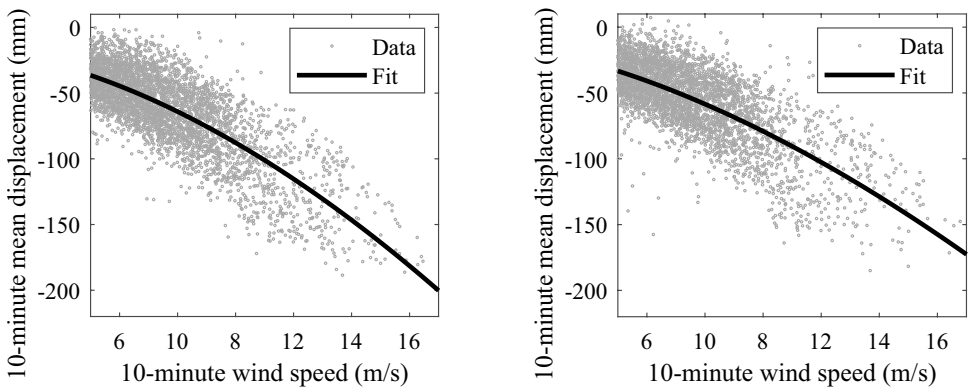

Fig. 21 Wind-induced mid-span lateral displacement versus wind speed in the direction sector NNW

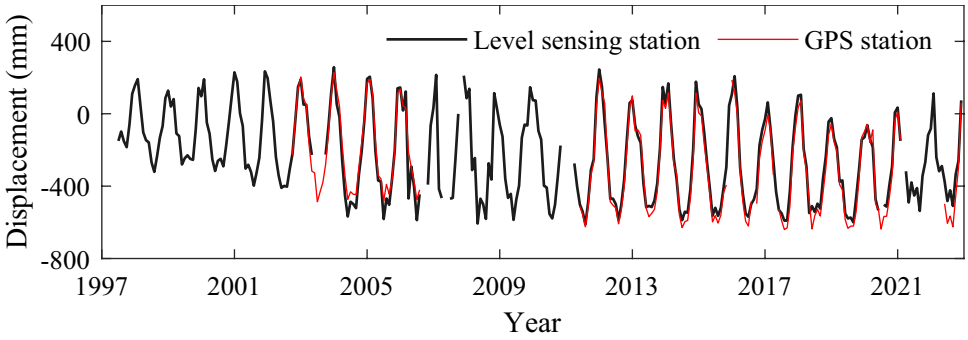

(a) Vertical displacement at the mid-span

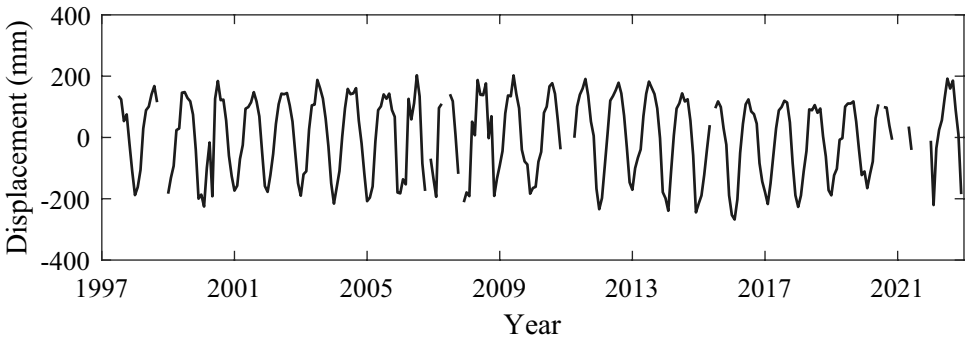

(b) Longitude displacement at the Tsing Yi abutment

Fig. 22 Monthly mean displacement of Tsing Ma Bridge in 1997–2022

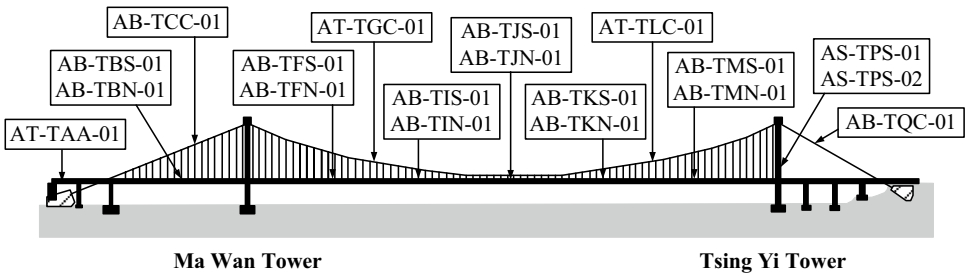

Fig. 23 Layout of the accelerometers on Tsing Ma Bridge

5.2.2 Relationship between frequency and temperature

Acceleration data are used to extract the dynamic properties of the bridge, including frequencies and mode shapes, through modal analysis [52]. Four days in different seasons in 2018 (6 February, 16 April, 2 August, and 21 November) are chosen to explore the relationship between the frequencies and effective temperature. Figure 24 plots the first four vertical and two lateral modal frequencies. Given that different modal frequencies differ in magnitude, each frequency is normalized by dividing its initial value. Vertical and lateral frequencies decrease as the effective temperature increases. The vertical frequency ratio slope against temperature is -1.7×10^{-4}/°C, approaching half the steel modulus temperature coefficient (-3.6×10^{-4}/°C), which is consistent with that in previous research [53]. The lateral frequency ratio slope is -6.7×10^{-4}/°C. This result reflects the influence of the concrete towers, which have a temperature coefficient of modulus of -3.0×10^{-3}/°C.

5.2.3 Long-term variation of the frequency

Dynamic properties are closely associated with the stiffness of a structure. Therefore, the long-term variation in frequencies can be an indicator of bridge condition. The previous subsection showed that varying temperatures may affect the frequencies as well and should be removed. In this regard, the bridge deck acceleration responses between 2:00 and 4:00 in March to May from 2004 to 2022, when the bridge deck's effective temperatures ranged between 23 and 24 °C, are selected to calculate the natural frequencies of the bridge. This situation will minimize the effects of varying temperatures and traffic on the frequencies. In each year, the calculated frequencies are averaged. Figure 25 shows the

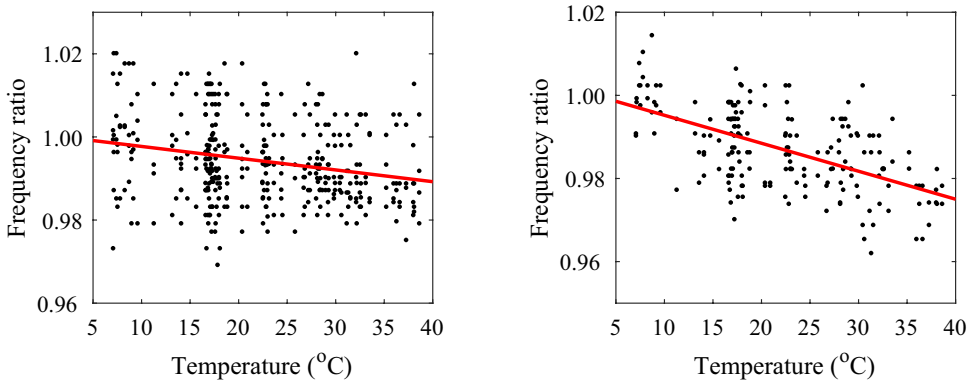

(a) Vertical modes (b) Lateral modes

Fig. 24 Relationship between bridge frequency and deck effective temperature

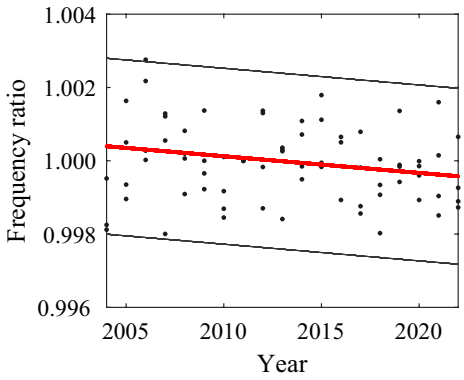

Fig. 25 Variations in the first four frequencies from 2004 to 2022

first four vertical frequency ratios versus the effective temperature from 2004 to 2022. The frequency ratios decrease at the ratio of -4.55×10^{-5}/year. The decrease rate is quite small and is neglectable.

5.3 Strain

5.3.1 Strain gauge layout

A total of 110 strain gauges have been installed on Tsing Ma Bridge. Figure 26 shows 44 single strain gauges, 62 pairs of strain gauges, and 4 rosette strain gauges, corresponding to "SS," "SP," and "SR," respectively. The sampling frequency was 25.6 Hz until 2002 and 51.2 Hz thereafter. Figure 27 shows two typical strain gauges underneath the railway beam and on the upper deck.

5.3.2 Long-term fatigue damage of the railway beam

Traffic-induced fatigue damage is a major defect of long-span steel suspension bridges [54, 55]. Therefore, strain responses of key components are analyzed to estimate the fatigue damage and predict the fatigue life resulting from the combined effects of railway and highway loads. The procedures specified in BS5400 Part 10 are followed [56]. The rainflow counting method and Miner' rule are adopted [55, 57].

Previous studies [57] have shown that railway loads dominate the fatigue damage of the main components of the bridge, particularly the bottom of the railway T-section beam, which undergoes significant train-induced responses. Sensor SS-TLS-13 was installed at the bottom of the railway T-section beam, as shown in Fig. 27. The railway beam experiences substantially larger strain ranges when trains are running on the bridge compared with no trains. This case allows the strains from trains and vehicles to be separated into two components. Using the strain response recorded on July 1, 2018 as an example, the fatigue damage caused by the train loads was 5.93×10^{-8}, approximately 98.50% of

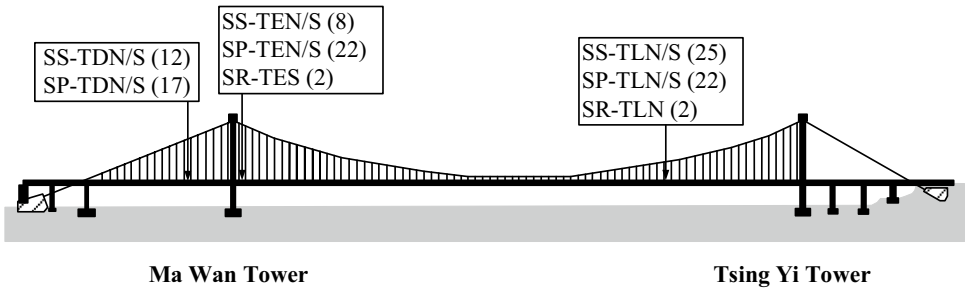

Fig. 26 Layout of the strain gauges on Tsing Ma Bridge

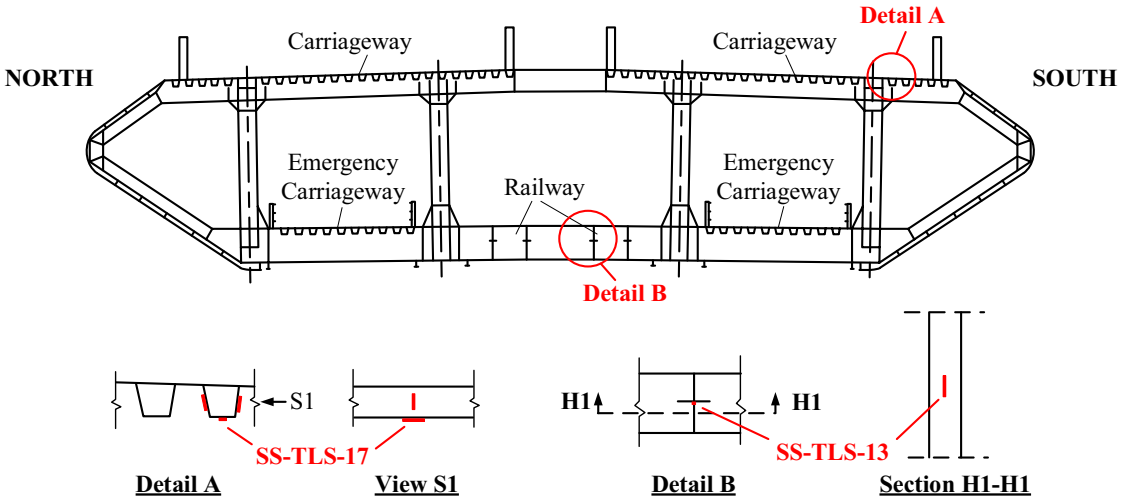

Fig. 27 Locations of sensors SS-TLS-17 and SS-TLS-13

the total combined damage from trains and vehicles. Therefore, railway beam fatigue damage is mainly caused by train loads.

Figure 28 shows the annual and cumulative fatigue damage of the railway beam at the sensor SS-TLS-13 from 1998 to 2022. By the end of 2022, the cumulative fatigue damage of the railway beam was about 0.026. If the annual number of trains and associated fatigue damage remain the same as 2019, the remaining fatigue life of the railway beam is predicted around 592 years. If the annual number of trains continues to increase at the rate of before 2022, then the remaining fatigue life is estimated to be about 194 years. In particular, the number of trains is unlikely to increase indefinitely. Nevertheless, even under the adverse scenario,

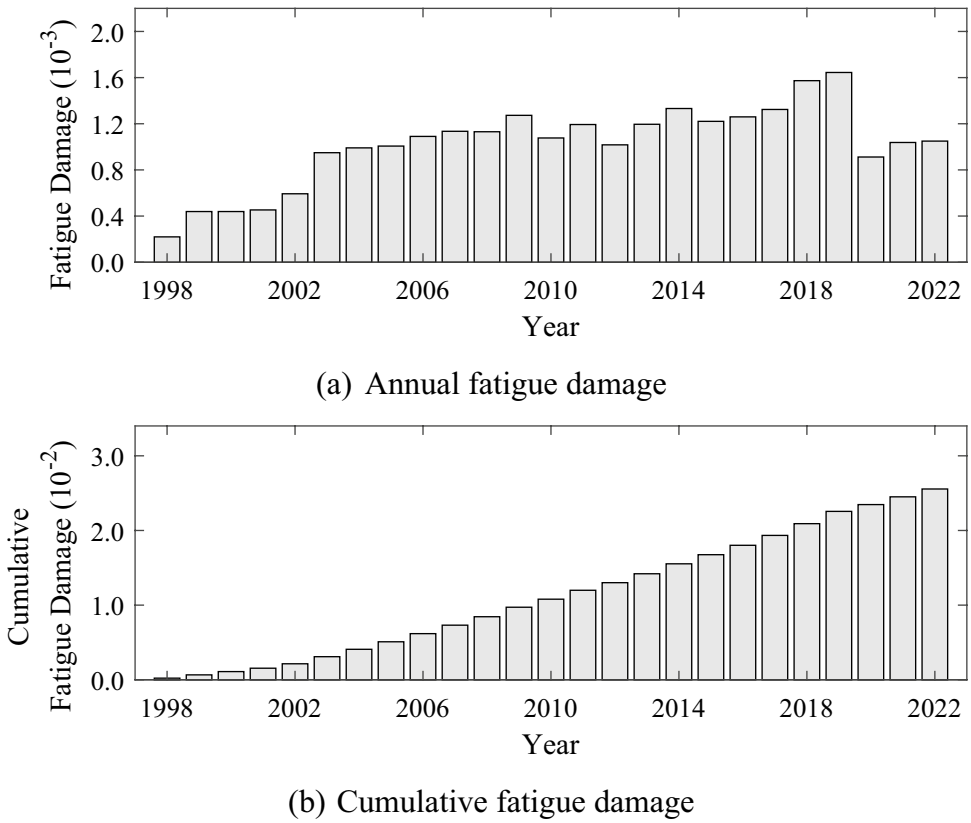

Fig. 28 Annual and cumulative fatigue damage of the railway T-section beam

the remaining fatigue life of the railway beam exceeds the 120-year design life.

5.3.3 Long-term fatigue damage of the upper orthotropic deck

Sensor SS-TLS-17, located on the bottom of the slow lane of upper orthotropic deck plate (Fig. 27), recorded the highest fatigue damage among all strain sensors. The deck strain from trains is opposite to the strain from vehicles, enabling the separation of strain induced by train and vehicle loads. Similarly, the strain responses recorded on July 1, 2018 show that the fatigue damage caused by vehicle loads was 6.60×10^{-7}, approximately 98.15% of the combined damage from trains and vehicles. This result indicates that fatigue damage of the upper orthotropic deck is mainly caused by vehicle loads.

The calculated annual and cumulative fatigue damage of the orthotropic deck at sensor SS-TLS-17 are presented in Fig. 29. The cumulative fatigue damage of the component keeps increasing from 1997 to 2022, and reaches approximately 0.271 by 2022. Continuous monitoring and appropriate measures if necessary will be conducted. For example, two long-span bridges in the area are under design to alleviate the traffic volume on Tsing Ma Bridge and deal with the new development of the Lantau Tomorrow Vision.

Note that the welds of the orthotropic deck, such as the trough–plate interface, are susceptible to fatigue damage from the repetitive traffic loads. Their strains cannot be measured using the present SHM system and can be simulated using numerical analysis, which is beyond the scope of this research.

6 Conclusions

The behavior of the Tsing Ma Bridge and the operational status of its SHM system raise widespread concerns. Field monitoring data over the past 26 years are analyzed to investigate the long-term bridge loads and responses. The current status and recent update of the SHM system are also discussed. The following conclusions can be drawn from this study:

(1) Sensors in the SHM system are generally in good operating condition, with all anemometers and displacement transducers remaining undamaged by 2022. The status of the GPS stations and thermometers requires attention owing to the increase in damaged sensors. The data transmission system has been upgraded to a wireless system. The ship impact detection alarm and

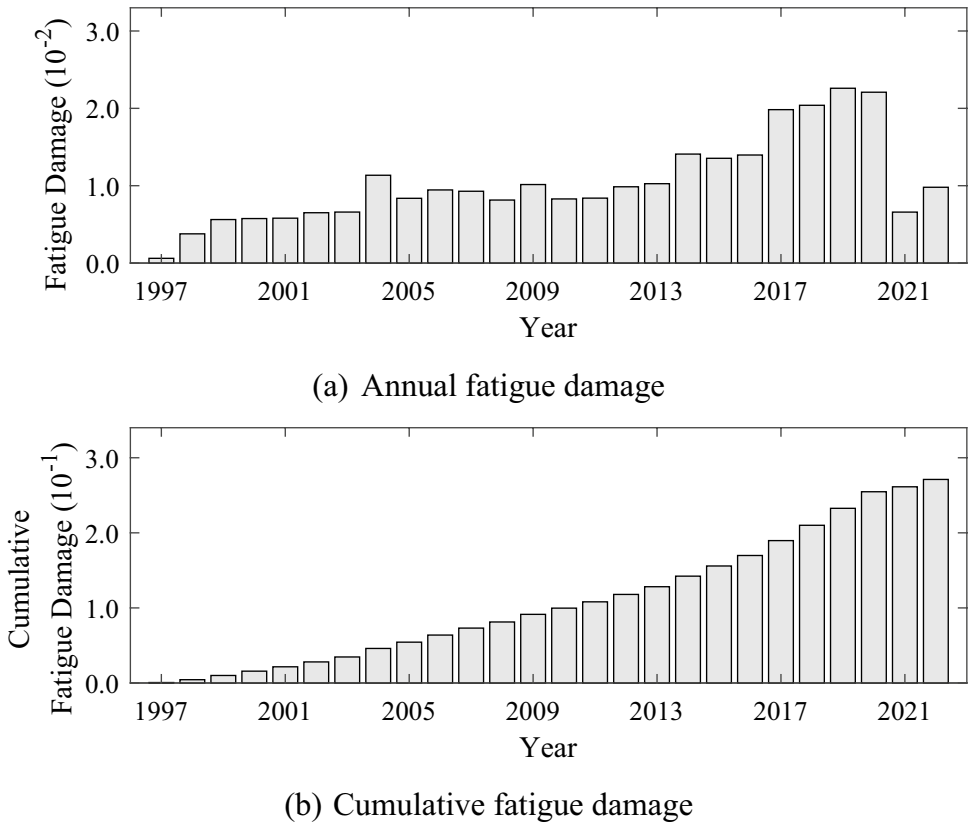

Fig. 29 Annual and cumulative fatigue damage of the upper orthotropic deck

acoustic monitoring systems have been integrated to the SHM system.

(2) The maximum and mean effective deck temperatures have increased at the rate of 0.51 °C/decade and 0.16 °C/decade, respectively, which are likely caused by global warming in the past decades. Moreover, the maximum effective temperature of the bridge deck approaches the design value. The deflection at the mid-span and longitudinal displacement of the deck end have a linear regression with temperature variation. Frequencies of the bridge decrease with an increase in the effective deck temperature.

(3) The predominant wind directions for typhoons and monsoons are NE and ESE. The Weibull PDF of monsoon winds shows no significant directional features. Monsoon wind speeds show a decreasing trend and have become markedly dispersed and variable. Typhoon speeds are concentrated within the range below 10 m/s. Moreover, there is no significant trend in typhoon speeds, while the duration increased by 2.5 h/year until 2022. For the relationship between wind and bridge responses, the 10-min mean wind speeds are proportional to the square of the lateral displacements of the deck and cables.

(4) During 2004 to 2022, the first four natural frequencies of the bridge remained almost unchanged with a neglectable decrease rate of -4.55×10^{-5}/year, indicating that the overall condition of the bridge is very good.

(5) Both railway and vehicle traffic have increased since 1997 and decreased thereafter from 2020 to 2022. As of 2019, the number of vehicles and trains stands at about 3 and 4 times the 1998 and 1999 levels, respectively. The analysis shows that the fatigue damage of the main component is primarily caused by trains, while fatigue of the orthotropic deck is mainly caused by highway vehicles.

7 Discussion and suggestions

The findings in this research underscore the significant benefits of long-term SHM in ensuring the safety and serviceability of long-span bridges. Without the SHM system, identifying these issues would be challenging or less convincing. With the continued development of bridge SHM systems in Hong Kong, several key enhancements should be made in the future.

(1) Expansion of sensor networks. Future SHM systems should expand their sensor networks to include a markedly comprehensive set of monitoring capabilities. This undertaking should incorporate corrosion sensors, pyranometers for solar radiation measurement and consider the effects of climate change [58], and hygrometers to monitor moisture levels, particularly for critical bridge components, such as cables.

(2) Integration of SHM and inspection data. Combining the real-time SHM data with regular bridge inspection findings can provide a markedly complete understanding of the overall bridge conditions. This endeavor will enable bridge operators to develop considerably comprehensive maintenance strategies based on the structural performance data and physical inspection observations.

(3) Incorporation of climate change adaptations. Bridge life cycle assessments should integrate climate change projections and scenarios to substantially understand the long-term impact on structural performance. Future SHM should also develop decision-making tools to provide appropriate repair and strengthening strategies to enhance the climate change resilience of bridges.

(4) Integration of advanced technologies. Advanced technologies such as AI and can improve the efficiency of SHM systems and also to reduce costs by analyzing data and detecting anomalies in real time, and DT technology can provide a virtual model of the bridge for more accurate simulations and predictions.

(5) Optimization of the SHM system. The SHM system was designed and implemented in the early 1990s, pioneering the technology in bridge engineering. Determining the number and type of sensors was challenging in that era. From the 25 years of SHM experience with the bridge, the following advice can be considered in the SHM system in the future.

(6) Level sensing stations can be removed as the GPS stations provide stable deformation in three directions. Level sensing stations of the Tsing Ma Bridge were designed in the 1990s, while GPS stations were added in 2002. The former may have the problem of liquid vaporization and is thus not commonly used now. Figure 22a shows that the two sets of sensors give similar results. Therefore, the removal of the level sensing stations is a natural choice. GPS has been criticized for the low accuracy of dynamic measurement. However, long-span bridges are usually flexible with low frequencies (the first 18 frequencies of the Tsing Ma Bridge are less than 0.38 Hz [9]). Their vibrations are generally significant and dominated by low frequencies. The GPS stations on the Tsing Ma Bridge have the precision of millimeters at the sampling rate of 10 Hz, which is adequate for dynamic displacement monitoring. Of course, if high-order modal properties are required, accelerometers are still the best choice compared to GPS.

(7) The number and the location of strain gauges can be updated. Fatigue damage is the most critical defect of

steel bridges with orthotropic decks. However, only a few strain gauges were installed on the orthotropic steel deck (Detail A in Fig. 27), while most were on the main components. More strain gauges should be placed close to the fatigue-critical components, e.g., rib-to-deck welds. Again, it is hard to determine the optimal position at the design stage because the actual behavior of the large-scale structure may differ from the numerical model.

Funding Open access funding provided by The Hong Kong Polytechnic University. This research was supported by the Research Grants Council – Collaborative Research Fund (Project No. C5004-23GF). The authors would like to thank the Hong Kong Highways Department for providing valuable data.

Declarations

Conflict of interest The authors have no relevant financial or non-financial interests to disclose.

References

1. Fujino Y, Siringoringo D (2013) Vibration mechanisms and controls of long-span bridges: a Review. Struct Eng Int 23(3):248–268. https://doi.org/10.2749/101686613X13439149156886
2. Saroufim A, Issa MA, Issa MA (2024) Optimized finite element analysis and strengthening assessment of the I-39 Kishwaukee bridge utilizing proof load testing. J Civ Struct Health Monit 14(3):545–574. https://doi.org/10.1007/s13349-023-00736-y
3. Li H, Ou J (2016) The state of the art in structural health monitoring of cable-stayed bridges. J Civ Struct Health Monit 6(1):43–67. https://doi.org/10.1007/s13349-015-0115-x
4. Le Ngo HM, Hashimoto K, Ha MT, Kita S, Fukada S, Ueno T (2023) Health assessment and self-powered corrosion monitoring system for deteriorated bridges. J Civ Struct Health Monit 13(2–3):799–810. https://doi.org/10.1007/s13349-023-00678-5
5. Pines D, Aktan AE (2002) Status of structural health monitoring of long-span bridges in the United States. Prog Struct Eng Mater 4(4):372–380. https://doi.org/10.1002/pse.129
6. ASCE (2021) Report card for America's infrastructure. American Society Of Civil Engineers, Reston
7. Washer GA (1998) Developments for the non-destructive evaluation of highway bridges in the USA. NDT E Int 31(4):245–249. https://doi.org/10.1016/S0963-8695(98)00009-7
8. Ko JM, Ni YQ (2005) Technology developments in structural health monitoring of large-scale bridges. Eng Struct 27(12):1715–1725. https://doi.org/10.1016/j.engstruct.2005.02.021
9. Xu YL, Xia Y (2012) Structural health monitoring of long-span suspension bridges. CRC Press
10. Memisoglu Apaydin N, Zulfikar AC, Cetindemir O (2022) Structural health monitoring systems of long-span bridges in Turkey and lessons learned from experienced extreme events. J Civ Struct Health Monit 12(6):1375–1412. https://doi.org/10.1007/s13349-022-00551-x
11. Bai Y, Demir A, Yilmaz A, Sezen H (2024) Assessment and monitoring of bridges using various camera placements and structural analysis. J Civ Struct Health Monit 14(2):321–337. https://doi.org/10.1007/s13349-023-00720-6
12. Lorenz R, Petryna Y, Lubitz C, Lang O, Wegener V (2024) Thermal deformation monitoring of a highway bridge: combined analysis of geodetic and satellite-based InSAR measurements with structural simulations. J Civ Struct Health Monit. https://doi.org/10.1007/s13349-024-00779-9
13. Bado MF, Casas JR (2021) A review of recent distributed optical fiber sensors applications for civil engineering structural health monitoring. Sensors 21(5):1818. https://doi.org/10.3390/s21051818
14. Dong C, Catbas FN (2021) A review of computer vision-based structural health monitoring at local and global levels. Struct Control Hlth 20(2):692–743. https://doi.org/10.1177/1475921720935585
15. Yu J, Meng X, Yan B, Xu B, Fan Q, Xie Y (2019) Global Navigation Satellite System-based positioning technology for structural health monitoring: a review. Struct Control Health 27(1):e2467. https://doi.org/10.1002/stc.2467
16. Zhang L, Qiu G, Chen Z (2021) Structural health monitoring methods of cables in cable-stayed bridge: a review. Measurement 168:108343. https://doi.org/10.1016/j.measurement.2020.108343
17. Gatti M (2019) Structural health monitoring of an operational bridge: a case study. Eng Struct 195:200–209. https://doi.org/10.1016/j.engstruct.2019.05.102
18. Wang F, Xu YL (2019) Traffic load simulation for long-span suspension bridges. J Bridge Eng 24(5):05019005. https://doi.org/10.1061/(ASCE)BE.1943-5592.0001381
19. Xu YL (2013) Wind effects on cable-supported bridges. Wiley
20. Frangopol DM, Liub M (2007) Structure and infrastructure engineering: maintenance, management, life-cycle design and performance. Struct Infrastruct Eng 7(6):389–413. https://doi.org/10.1080/15732470600591117
21. Li H, Ou J, Zhao X, Zhou W, Li H, Zhou Z (2006) Structural health monitoring system for the Shandong Binzhou Yellow River Highway Bridge. Comput-Aided Civ Infrastruct Eng 21(4):306–317. https://doi.org/10.1111/j.1467-8667.2006.00437.x
22. Wang H, Tao T, Li A, Zhang Y (2016) Structural health monitoring system for Sutong cable-stayed bridge. Smart Struct Syst 18(2):317–334. https://doi.org/10.12989/sss.2016.18.2.317
23. Wang H, Li A, Guo T, Tao T (2014) Establishment and application of the wind and structural health monitoring system for the Runyang Yangtze River Bridge. Shock Vib 2014:1–15. https://doi.org/10.1155/2014/421038
24. Yan Y, Mao X, Wang X, Yu X, Fang L (2019) Design and implementation of a structural health monitoring system for a large sea-crossing project with bridges and tunnel. Shock Vib 2019:2832089. https://doi.org/10.1155/2019/2832089
25. Fujino Y, Murata M, Okano S, Takeguchi M (2000) Monitoring system of the Akashi Kaikyo Bridge and displacement measurement using GPS. SPIE, Bellingham, pp 229–236. https://doi.org/10.1117/12.387814

26. Soman R, Kyriakides M, Onoufriou T, Ostachowicz W (2018) Numerical evaluation of multi-metric data fusion based structural health monitoring of long span bridge structures. Struct Infrastruct Eng 14(6):673–684. https://doi.org/10.1080/15732479.2017.1350984
27. Abdel-Ghaffar AM, Scanlan RH (1985) Ambient vibration studies of golden gate bridge: I. Suspended structure. J Eng Mech 4(111):463–482. https://doi.org/10.1061/(ASCE)0733-9399(1985)111:4(463)
28. Zhu YF, Ren WX, Wang YF (2022) Structural health monitoring on yangluo Yangtze River bridge: implementation and demonstration. Adv Struct Eng 25(7):1431–1448. https://doi.org/10.1177/13694332211069508
29. Zhu S, Xu YL, Wong K, Zheng Y (2011) Diagnosis and prognosis of Stonecutters Bridges based on structural health monitoring system. In: Proceedings of the 5th international conference on structural health monitoring of intelligent infrastructure. México
30. Fogleson M (2021) The 2021 outstanding civil engineering achievement awards. Civ Eng Mag Arch 9(6):46–51. https://doi.org/10.1061/ciegag.0001594
31. Wong KY, Lau CK, Flint AR. Planning and implementation of the structural health monitoring system for cable-supported bridges in Hong Kong. In: Nondestructive evaluation of highways, utilities, and pipelines IV, pp 266–275. https://doi.org/10.1117/12.387819
32. Xu Y (2018) Making good use of structural health monitoring systems of long-span cable-supported bridges. J Civ Struct Health Monit 8(3):477–497. https://doi.org/10.1007/s13349-018-0279-2
33. Ni Y, Wong KL (2012) Integrating bridge structural health monitoring and condition-based maintenance management. In: 4th international workshop on civil structural health monitoring. Berlin
34. Mahmoud K (2006) Advances in cable-supported bridges: selected papers, 5th international cable-supported bridge operator's conference. CRC Press
35. Feng MQ, Leung RY, Eckersley CM (2020) Non-contact vehicle weigh-in-motion using computer vision. Measurement 153:107415. https://doi.org/10.1016/j.measurement.2019.107415
36. Ge L, Dan D, Liu Z, Ruan X (2022) Intelligent simulation method of bridge traffic flow load combining machine vision and weigh-in-motion monitoring. IEEE trans Intell Transp Syst 23(9):15313–15328
37. He W, Liu J, Song S, Liu P (2024) A non-contact vehicle weighing approach based on bridge weigh-in-motion framework and computer vision techniques. Measurement 225:113994. https://doi.org/10.1016/j.measurement.2023.113994
38. Wang X, Wu W, Du Y, Cao J, Chen Q, Xia Y (2023) Wireless IoT monitoring system in Hong Kong–Zhuhai–Macao Bridge and edge computing for anomaly detection. IEEE Internet Things J 11(3):4763–4774
39. Zhang Y, Wang X, Ding Z, Du Y, Xia Y (2022) Anomaly detection of sensor faults and extreme events based on support vector data description. Struct Control Health. https://doi.org/10.1002/stc.3047
40. Beard AS, Young JS (1995) Aspects of the design of the Tsing Ma bridge. In: Bridges into the 21st century, pp 93–100
41. Wong K (2004) Instrumentation and health monitoring of cable-supported bridges. Struct Control Health 11(2):91–124. https://doi.org/10.1002/stc.33
42. Xu YL, Chen B, Ng CL, Wong KY, Chan WY (2009) Monitoring temperature effect on a long suspension bridge. Struct Control Health 17:632–653. https://doi.org/10.1002/stc.340
43. Chen ZW, Xu YL, Li Q, Wu DJ (2011) Dynamic stress analysis of long suspension bridges under wind, railway, and highway loadings. J Bridge Eng 16:383–391. https://doi.org/10.1061/(ASCE)BE.1943-5592.0000216
44. Xu YL (2016) SHM-based fatigue damage prognosis for long-span cable-supported bridges under multiple dynamic loadings. In: Maintenance, monitoring, safety, risk and resilience of bridges and bridge networks. CRC Press/Belkema, pp 131–145
45. Xia Q, Zhang J, Tian Y, Zhang Y (2017) Experimental study of thermal effects on a long-span suspension bridge. J Bridge Eng 22(7):04017034. https://doi.org/10.1061/(ASCE)BE.1943-5592.0001083
46. Zhu Q, Wang H, Mao J, Wan H, Zheng W, Zhang Y (2020) Investigation of temperature effects on steel-truss bridge based on long-term monitoring data: case study. J Bridge Eng 25(9):05020007. https://doi.org/10.1061/(ASCE)BE.1943-5592.0001593
47. Bayraktar A, Akköse M, Taş Y, Erdiş A, Kurşun A (2022) Long-term strain behavior of in-service cable-stayed bridges under temperature variations. J Civ Struct Health Monit 12(4):833–844. https://doi.org/10.1007/s13349-022-00578-0
48. Xia Y, Chen B, Zhou X, Xu Y (2013) Field monitoring and numerical analysis of Tsing Ma Suspension Bridge temperature behavior. Struct Control Health 20(4):560–575. https://doi.org/10.1002/stc.515
49. IPCC (2021) Summary for policymakers. In: Masson-Delmotte VP, Zhai A, Pirani SL, Connors C, Péan S, Berger N, Caud Y, Chen L, Goldfarb MI, Gomis M, Huang K, Leitzell E, Lonnoy JBR, Matthews TK, Maycock T, Waterfield O, Yelekçi, Yu R, Zhou B (eds) Climate change 2021: the physical science basis. Contribution of Working Group I to the sixth assessment report of the Intergovernmental Panel on Climate Change
50. Lee B, Lee T (2010) The monsoons and climate change. Hong Kong Observatory. https://www.hko.gov.hk/en/education/weather/monsoons/00072-the-monsoons-and-climate-change.html
51. Zhou Y, Xia Y, Chen B, Fujino Y (2020) Analytical solution to temperature-induced deformation of suspension bridges. Mech Syst Signal Process 139:106568. https://doi.org/10.1016/j.ymssp.2019.106568
52. Fu Z, He J (2001) Modal analysis. Elsevier
53. Xia Y, Chen B, Weng S, Ni Y, Xu Y (2012) Temperature effect on vibration properties of civil structures: a literature review and case studies. J Civ Struct Health Monit 2(1):29–46. https://doi.org/10.1007/s13349-011-0015-7
54. Chen ZW, Xu YL (2012) SHMS-based fatigue reliability analysis of multiloading suspension bridges. J Bridge Eng 138:299–307. https://doi.org/10.1061/(ASCE)ST.1943-541X.0000460
55. Ye XW, Ni YQ, Wong KY, Ko JM (2012) Statistical analysis of stress spectra for fatigue life assessment of steel bridges with structural health monitoring data. Eng Struct 45:166–176. https://doi.org/10.1016/j.engstruct.2012.06.016
56. BS (1980) BS5400: part 10, code of practice for fatigue. British Standards Institution, London
57. Chen ZW, Xu YL, Xia Y, Li Q, Wong KY (2011) Fatigue analysis of long-span suspension bridges under multiple loading: Case study. Eng Struct 33(12):3246–3256. https://doi.org/10.1016/j.engstruct.2011.08.027
58. Zhang L, Shan Y, Li L, Wang F, Xia Y (2024) Thermal boundary conditions for heat transfer analysis of bridges considering non-uniform distribution of internal air temperature by computational fluid dynamics. J Civ Struct Health Monit 14(5):1295–1310. https://doi.org/10.1007/s13349-024-00795-9